Lasers in Surgery and Medicine 50:213–221 (2018)

Multifunctional In Vivo Imaging For Monitoring Wound Healing Using Swept-Source Polarization-Sensitive Optical Coherence Tomography

Kwan S. Park, PhD, Woo June Choi, PhD, Shaozhen Song, PhD, Jingjiang Xu, PhD, and Ruikang K. Wang, PhD*
Department of Bioengineering, University of Washington, Seattle, Washington 98195

Background and Objective: Wound healing involves a complex and dynamic biological process in response to tissue injury. Monitoring of the cascade of cellular events is useful for wound management and treatment. The aim of this study is to demonstrate the potential of multifunctional polarization-sensitive optical coherence tomography (PS-OCT) to longitudinally monitor the self-healing process in a murine cutaneous wound model.
Materials and Methods: A multi-functional PS-OCT system based on swept source OCT configuration (1,310 nm central wavelength) was designed to obtain simultaneously microstructural, blood perfusion, and birefringent information of a biological tissue *in vivo*. A 1-mm-diameter wound was generated in a mouse pinna with a complete biopsy punch. Afterwards, the self-healing process of the injured tissue was observed every week over 6-week period using the multifunctional system to measure changes in the tissue birefringence. Further OCT angiography (OCTA) was used in post data processing to obtain blood perfusion information over the injured tissue.
Results: Three complementary images indicating the changes in anatomical, vascular, and birefringent information of tissue around wound were simultaneously provided from a 3-dimensional (3-D) PS-OCT data set during the wound repair over 1 month. Specifically, inflammatory and proliferative phases of wound healing were characterized by thickened epidermal tissue (from OCT images) and angiogenesis (from OCT angiography images) around wound. Also, it was observed that the regenerating tissues had highly realigned birefringent structures (from PS-OCT images).
Conclusion: This preliminary study suggests that the proposed multi-functional imaging modality has a great potential to improve the understanding of wound healing through non-invasive, serial monitoring of vascular and tissue responses to injury. Lasers Surg. Med. 50:213–221, 2018. © 2017 Wiley Periodicals, Inc.

Key words: multifunctional imaging; PS-OCT; OCT angiography; wound healing; blood vessels; birefringence; collagen

INTRODUCTION

Since optical coherence tomography (OCT) has been developed in 1991, substantial progress has been made in terms of its imaging speed, resolution, imaging depth, and system sensitivity [1,2]. Benefiting from its non-invasive and non-contact imaging ability of depth-resolved tissue anatomy at a micrometer scale, OCT has demonstrated its usefulness in a variety of medical applications including ophthalmology [3], dermatology [4,5], dentistry [6], neurology [7], cardiology [8], and gastrointestinal imaging [9].

In recent years, functional extensions to OCT have become an increasingly common strategy to collect supplementary information of the sample under investigation, in addition to its morphological information, for further comprehensive examination. Various technologies are utilized to extend the contrast mechanism of OCT from simply optical scattering contrast to a wide range of modalities, such as blood flow contrast, optical polarization contrast, and mechanical property contrast. The functional extension has enabled OCT to interrogate blood perfusion and blood flow with OCT angiography (OCTA) [10–12] and Doppler OCT (DOCT) [13,14], molecular properties with spectroscopic OCT (SOCT) [15,16], or elastic properties of tissues with optical coherence elastography (OCE) [17–20]. Up to now, these diverse functional variants of OCT have led to continuous improvement of system development, thereby its increased scope of biomedical applications. Especially, since it is known that disorder in tissue microcirculation is linked to many diseases in dermatology, ophthalmology, and neurology, OCT microvascular imaging has received great attention in the field of biomedical research. OCTA visualized perfused vasculature of microcirculatory tissues without a need for contrast agents, which can be useful in studying diseases where the microvascular morphology changes over time. OCTA enhances motion-contrast of red blood cells (RBCs) by

Conflict of Interest Disclosures: All authors have completed and submitted the ICMJE Form for Disclosure of Potential Conflicts of Interest and have disclosed the following: The authors state no financial conflict of interest on this study.
Contract grant sponsor: National Institutes of Health; Contract grant numbers: R01EB009682, R01HL093140.
*Correspondence to: Dr. Ruikang K. Wang, Department of Bioengineering, University of Washington, 3720 15th Ave NE, Seattle, WA 98195. E-mail: wangrk@uw.edu
Accepted 3 November 2017
Published online 30 November 2017 in Wiley Online Library (wileyonlinelibrary.com).
DOI 10.1002/lsm.22767

detecting changes in either amplitude or phase, or both of OCT signals to selectively highlight the vessels. Since arguably the first introduction of three-dimensional (3-D) OCTA in 2007 [21], there has been an intense technical advance in methodologies of mapping vascular perfusion, tone, flow, and speed down to capillary level [22].

Polarization-sensitive OCT (PS-OCT) is one of the functional extensions of OCT, providing polarization-sensitive (PS) images as well as structural information regarding the sample [23–25]. *PS* contrast is generated by the changes in polarization of OCT light into optically anisotropic materials whereby the two orthogonal polarization components of propagating light wave are relatively retarded due to birefringence responsible for phenomenon of double refraction. For biological tissues, the polarization change is induced by tissue birefringence, which mainly comes from the distribution of fibrous collagen in the skin. Using the collagen-induced *PS* contrast, PS-OCT has extended its application in dermatology such as burn depth estimation [26,27] and human scar assessment [28,29]. There are other imaging techniques currently available for assessing skin injuries, for example laser speckle imaging and spatial frequency domain imaging [30–34]. However, they are not amenable to investigate depth information of the skin tissue injury.

The collagen in tissues plays an important role in skin wound healing. For example, quantification of the cutaneous wound healing using PS-OCT has been first reported in 2006 [35]. This study indicated that the specific timing of birefringent change in a biopsy punched wound on rabbit pinna is correlated to the healing phase during wound healing, and moreover, the use of drugs affects the specific timing of the change in birefringence. Individually, recent OCTA studies have reported explicit microcirculation dynamics during cutaneous wound healing phase in small animals *in vivo* [36–38]. These two functional information (birefringence and blood flow) is complementary and informative, and therefore, the combination of these two OCT technologies (PS-OCT and OCTA) would be useful for better understanding of the wound healing in tissues. In this paper, hence, we present multifunctional PS-OCT to observe cutaneous wound healing of a mouse ear pinna. Images of structure, birefringence, collagen orientation change, and blood vessels are obtained and analyzed. Although a few of multifunctional PS-OCT studies have been reported to examine birefringence and blood vessels in human skin [39–41] and eyes [42,43], no reports have demonstrated assessments in tissue birefringence and microcirculatory response to wound in healing.

SYSTEM SETUP AND METHODS

System Design

The system configuration is analogous to typical polarization-maintaining (PM) single mode fiber based swept-source PS-OCT [44]. Figure 1 shows a schematic of the experimental setup. A light source was a MEMS tunable VCSEL swept-laser (Thorlabs, Inc., Newton, NJ) operating at 1,310 nm central wavelength with a sweeping rate of 100 kHz. All of optical fibers used in the system were PM fibers. The light from the source was linearly polarized by a linear polarizer (LP) and become circular polarized light by a quarter wave plate (QWP) installed in sample arm, illuminating the sample. In the reference arm, the linear polarized light passed through another QWP oriented at 22.5 degrees to the incident light. Then retro-reflected light become linear polarized light oriented at 45 degrees to the slow axis of the PM fiber to have same intensity in the slow and fast axis of the PM fiber. Light coming back from both reference and sample arms were recombined and interfered at a polarization maintaining coupler (PMC), and then one routed to a polarization beam splitter1 (PBS1) *via* circulator and the other, went to a PBS2. Here, optical path length between two beams from the PMC to the PBS1 and the PBS2 were adjusted to have the same fiber length to avoid phase mismatch of the interference signals detected by two balanced photo-detectors (BPDs). After that, interference signals detected by each BPD were low pass filtered and sampled by a data acquisition (DAQ) card. The sampling clock is provided by the MZI optical clock module in the laser source, operating at around 450 MS/s. To control the timing of data acquisition and XY galvo scanners, sweep start trigger signal from the laser was used as a trigger for DAQ card and timing-signal for a functional generator controlling the XY scanner. In the PM fibers of reference and sample arms, a polarization cross coupling between the light waves at the fast and slow axis can occur by the imperfection of polarized optics and fiber axis misalignment at the fiber connection interfaces, typically yielding large-amplitude crosstalk signals. Because the polarization crosstalk signals can overlay with OCT signals from the tissue, it deteriorates the final PS-OCT image quality [45]. To solve the crosstalk issue, we extended the length of PM fibers in each arm up to 30 m that could shift the crosstalk signal band away from the original OCT signals [44]. The sensitivity of the system was measured to be ~103 dB with ~3 mW incident light power of the sample and a 30 dB neutral density filter. The spatial resolution of the system was measured to be 22 μm (axial) $\times$ 22 μm (lateral).

Scanning Protocol and Post-Processing of Data

In all the experiments, 3-D OCT data were acquired by step-scanning of XY scanners in the sample arm; 450 A-lines were captured along the fast X-axis to obtain one cross-sectional B-scan image and the fast B-scan was 10 times repeated in the same position. The repetitive B-scan manner was then conducted at 450 different locations along the Y-axis, producing a total 4,500 B-frames in a cubic dataset. The scanned tissue area was 5 mm $\times$ 5 mm in XY direction, corresponding to 11 μm spatial interval of each scan position.

A PS-OCT dataset is composed of two sets of 4,500 B-frames, which are horizontal and vertical polarization components detected by two BPDs, respectively. OCTA (vessel) and PS-OCT (reflectivity, phase retardation, and relative axis orientation) images are generated by

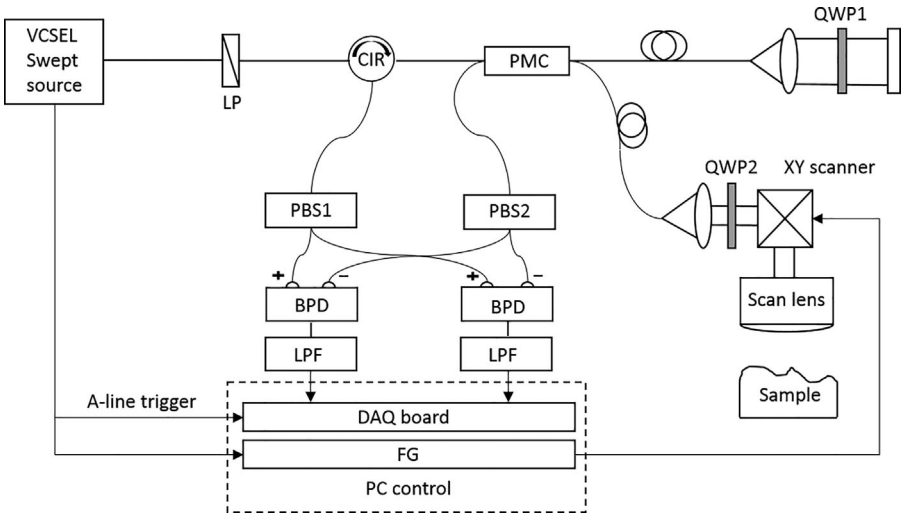

Fig. 1. Schematic of the PM fiber based PS-OCT system setup. LP: linear polarizer; CIR: polarization maintaining circulator; PMC: polarization maintaining coupler; QWP#: quarter wave plate; PBS#: polarization beam splitter; BPD: balanced photodetector; LPF: low pass filter; DAQ: data acquisition board; FG: functional generator.

post-processing. In this study, we used optical microangiography (OMAG), a complex signal-based OCTA method to contrast the functional blood vessels within the scanned tissue volume [46,47]. Unlike intensity-based OCTA, OMAG is more sensitive to slow flows. With OCT data obtained at each channel, two blood perfusion images were computed using the OMAG algorithm and averaged to form one OMAG image. Eventually, one 3-D OMAG image set was constructed and then collapsed into a 2-D *en face* image through maximum intensity projection (MIP). The reflectivity (R), phase retardation (δ), and relative axis orientation (θ) images are obtained using the following relations [48]:

$$R(z) \sim A_H^2(z) + A_V^2(z), \tag{1}$$

$$\delta(z) = \arctan[A_V(z)/A_H(z)], \tag{2}$$

$$\theta = (\pi - \Delta\Phi)/2, \tag{3}$$

where A_H and A_V are the amplitude of horizontal and vertical channels, and $\Delta\Phi$ is the phase difference between vertical and horizontal channels.

Wound Induction and Imaging

In order to monitor wound healing of the tissue, we used a well-known biopsy punch wound model [36]. Briefly, a hairless young adult mouse (SKH-1E, 23 g) was prepared and its right ear pinna was flattened and immobilized on a glass plate using double-sided tape. To induce a wound on the pinna, a punch biopsy was performed on the dorsal side of pinna, yielding a 1-mm-diameter round hole through the tissue. After onset of the wound, then self-healing process of the wounded injury was observed using PS-OCT system at weekly interval over 6 weeks. In every imaging session, the mouse was placed on a heating pad and anesthetized to reduce the body motion during OCT imaging. The wound was gently covered by a 5-mm-diameter rounding cover glass to flatten the tissue surface between which was filled with index-matching mineral oil to avoid hyper-reflection at the glass and tissue surfaces [49,50]. The imaging was performed at a controlled room temperature ($\sim$23°C) which maintains the blood flow stable in peripheral vessels in the mouse ear. The experimental protocol was in compliance with federal guidelines for care and handling of small rodents and approved by the Institution Animal Care and Use Committee of the University of Washington, Seattle.

RESULTS

Wound healing is a process of tissue to repair itself after injury. Its healing stages can be categorized by four predictable phases: blood clotting (hemostasis), inflammation, tissue growth (proliferation), and tissue remodeling (maturation) [51]. We have observed the mouse pinna under wound healing for 41 days. Therefore, inflammation and proliferation of four phases would be mainly monitored with our multifunctional PS-OCT. In general, PS-OCT provides not only structural images but also phase retardation images and axis orientation images. Furthermore, blood vessel images can be obtained by incorporating OMAG technique into PS-OCT instrument. In Figure 2, two photographs in a top row show the same mouse pinna on 1- and 30-day after wound induction. Images along each row are representative multifunctional PS-OCT cross sections obtained from the wound site indicated by the black line in the photographs, showing reflectivity images, corresponding phase retardation images, axis orientation images, and blood vessel images in sequential. The

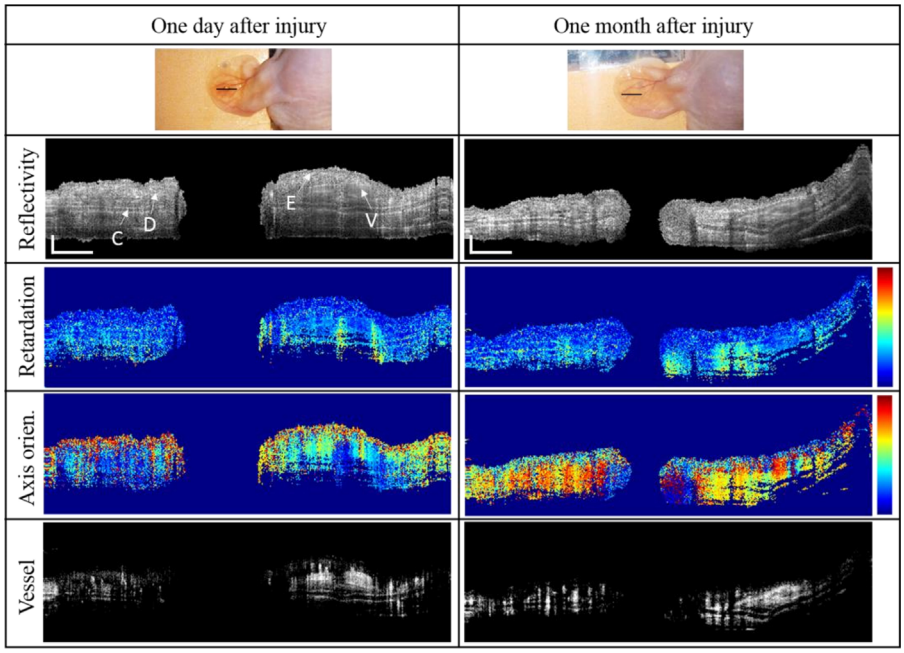

Fig. 2. Multifunctional PS-OCT imaging of the punch biopsy wound model of a hairless mouse *in vivo*. The imaging can simultaneously provide reflectivity, phase retardation, relative axis orientation, and vessel blood images of the wound site. Top row: photographs of the same mouse pinna 1 day (left) and 30 days (right) after wound induction. From second panel, left and right columns sequentially show reflectivity, phase retardation, axis orientation, and blood vessel cross-sections of the 1 and 30 days wound (taken from black solid lines [see top row]), respectively. E: epidermis layer; D: dermis layer; V: vessel; C: auricular cartilage. The white bar is 500 μm. Color scale of phase retardation and relative axis orientation are from 0° to 90° and from −90° to +90°, respectively.

reflectivity image shows anatomical alteration in the tissue after tissue injury. Epidermis (E) and dermis layers (D), blood vessel (V), and cartilage (C) in the tissue of the mouse pinna is observable in the reflectivity images. And blood vessels can be separately visualized in the blood vessel images by OMAG technique. The phase retardation image represents cumulative phase retardation due to the birefringence inside the tissue because the difference in phase shift between two characteristic polarization states of backscattered light from the tissue is altered by the tissue birefringence. The axis orientation image shows the fast axis orientation of the collagen fibers within the tissue, giving a directional information of fibrous collagen in the tissue. The vessel image offers blood perfusion information in the functional vessel.

Structural Change

Time-course structural changes in wound healing were confirmed from OCT images. Figure 3a shows maximum intensity projection images of OCT data sets taken at 0 days and 1, 8, 15, 21, 27, 36, and 41 days after wound induction. Figure 3b shows mean intensity projection image of the 3-D OCT dataset obtained on 41 days after wound induction and its cross-sectional images along two orthogonal lines (red and yellow lines). An outer dotted circle presented in the *en face* image indicates the initial wound area and an inner dotted circle is the border of repairing tissues on day 41. It was observed that the wound was significantly contracted and filled with new tissue (granulation tissue), and concurrently re-epithelialization of the epidermis occurred, providing the generation of new tissue, which is the typical characteristics of the proliferation stage of the wound healing phase. In the XY view of Figure 3b, the inner circle is distally biased to the outer circle, indicating that the tissue growth rate is much faster at the proximal wound site. It is apparent from the generated tissues in the XZ and YZ OCT cross-sections in Figure 3b, where white arrows point the wound boundary at day 0. We measured the widths of tissue growth from each white arrow at the right and left sides of the wound, respectively. The measurement was done at the halfway of open wound on each imaging day. Figure 3d shows the time-course change in widths of growing tissue at the right and left side of wound, indicating that the tissue width of the right side is two times larger than that on the left side since day 15 post-wounding. This asymmetry in local tissue growth during wound repair is probably due to the geometrical features of peripheral tissues (e.g., the closer to the major branch vessels, much easier for nutrition feeding). Figure 3c shows the thickness change of the wound surrounding tissue as a white box in Figure 3b, in which the thickness values were averaged. The thickness on 1 day after wounding was sharply increased and then gradually declined with time. Note that although the

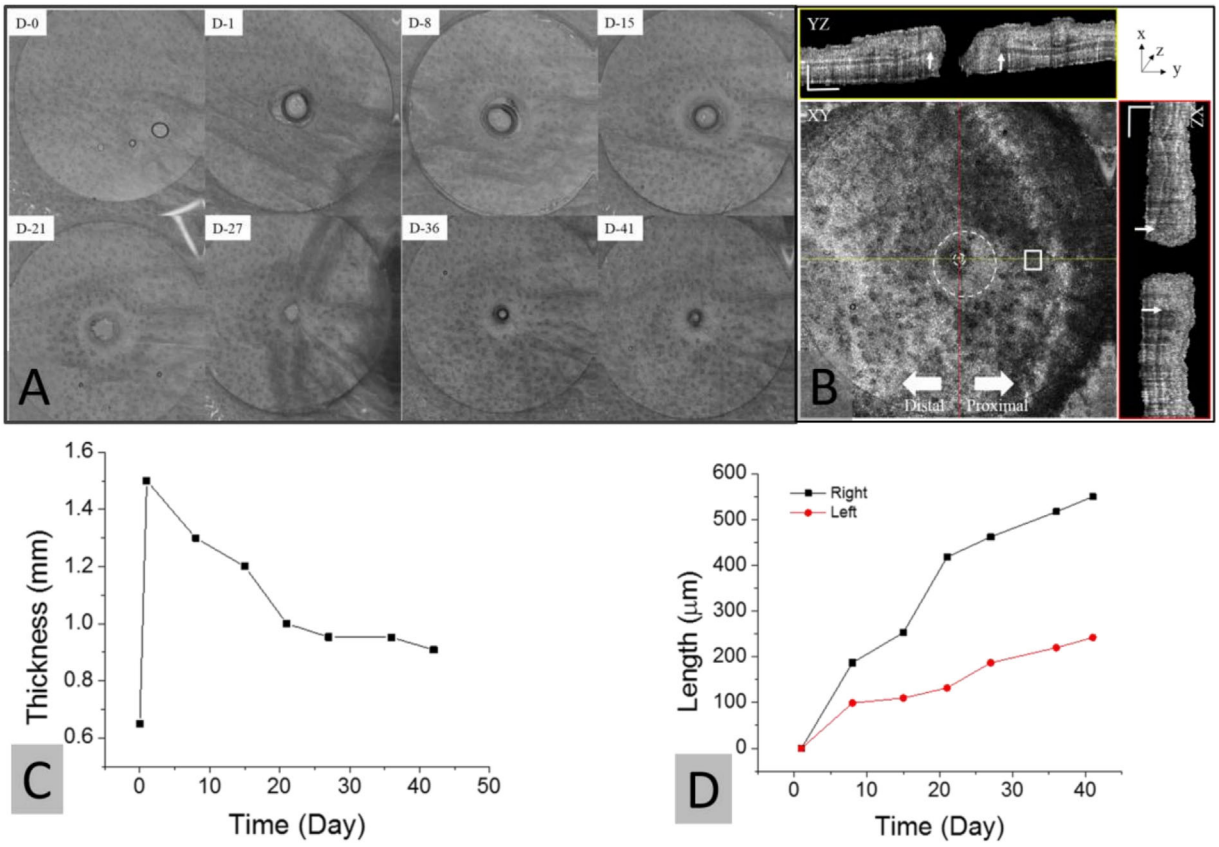

Fig. 3. Structural changes in the wound area in the mouse pinna with time and reflectivity images taken at 41 days after injury: (**a**) Maximum intensity projection of reflectivity datasets. (**b**) *En face* image at a certain depth and cross-sectional images along red and yellow lines. (**c**) Tissue thickness changes of the area indicated as a white square in (a) at different time points. (**d**) Regenerated tissue lengths in the YZ dimensions at different time points. The scale bar is 500 μm.

auricular cartilage gradually grows in wound healing, its regeneration rate is much slower than the tissue regenerations [52].

Time-Course in Blood Vessel Networks Around Ear Wound Site

OMAG algorithm was used to process the 3D PS-OCT datasets to obtain functional vascular networks within the scanned tissue volume. Figure 4a shows MIP images (5mm × 5 mm) of the 3-D vasculatures of mouse pinna taken at 0 days and 1, 8, 15, 21, 27, 36, and 41 days after the onset of wound. The field of view (FOV) of the obtained angiogram was $5 \times 5\,mm^2$. One-day image describes the vessel morphological change around the wound that obstructed a branch of major artery and vein just proximal to the bifurcation of the major vein. This induced a rapid increase in flow across the collaterals of the ear pinna, including the readily identifiable arterial vessel (white arrow). From 8 days post-wound, angiogenic capillary sprouts were observed surrounding the wound and the vessel density was gradually diminished during wound repair. The vessel diameter was also increased after injury as shown in Figure 4b, meaning that blood perfusion within the tissue area around wound increased. Figure 4b shows the changes in diameter of the vessel in a red circle with the times.

Polarization-Sensitive OCT Images

In addition to structural and vascular information, PS-OCT provides optical anisotropy of birefringent tissue, which is mainly characterized as a phase retardation and an axis orientation. The phase retardation and axis orientation changes in the wounded mouse pinna could be mapped at various dates with the *en face* mapping of 3D *PS* dataset at a depth above the cartilage, which are shown in Figure 5. In Figure 5, images in two rows from top show this *en face* mapping of the phase retardation data at 0–41 days post-wounding. In appearance, the phase retardation values surrounding wound site (indicated as white stars in Fig. 5) is increased after injury. It seems that the phenomenon of increasing birefringence correlates with the swelling and increased contortion of single collagen shown in inflammation tissues [53]. In addition, the phase retardation values at the regenerated tissues nearby wound site (indicated as a black arrowhead in Fig. 5) are low relative to the surrounding until

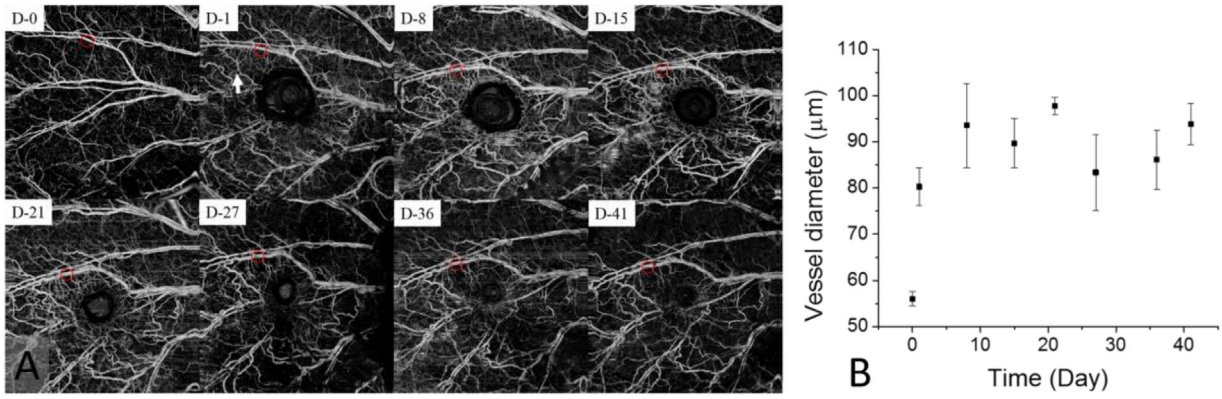

Fig. 4. OMAG images of mouse pinna from *in vivo* PS-OCT dataset at different time points (**a**) and corresponding changes in vessel diameter (**b**). FOV of images shown in (**a**) is $5 \times 5\,\text{mm}^2$.

21 days, but since then started to be increased with time while the wound being closed. A similar trend was shown in the relative axis orientation images at the bottom row in Figure 5, in which the directionality of axis orientation around the boundary of wound site has become distinct since 21 days post-wounding. It indicates that the phase retardation may be correlated to both of amount of collagen and the orientation of collagen fibers in the ear pinna dermis [35]. However, the formation of the higher phase retardation across the mouse ear pinna (indicated as white arrows in Fig. 5) might be interesting; with no wound (day 0), the phase retardation distribution is featured like strands, pronounced at the proximal region (right side in Fig. 5). The retardation post-wounding

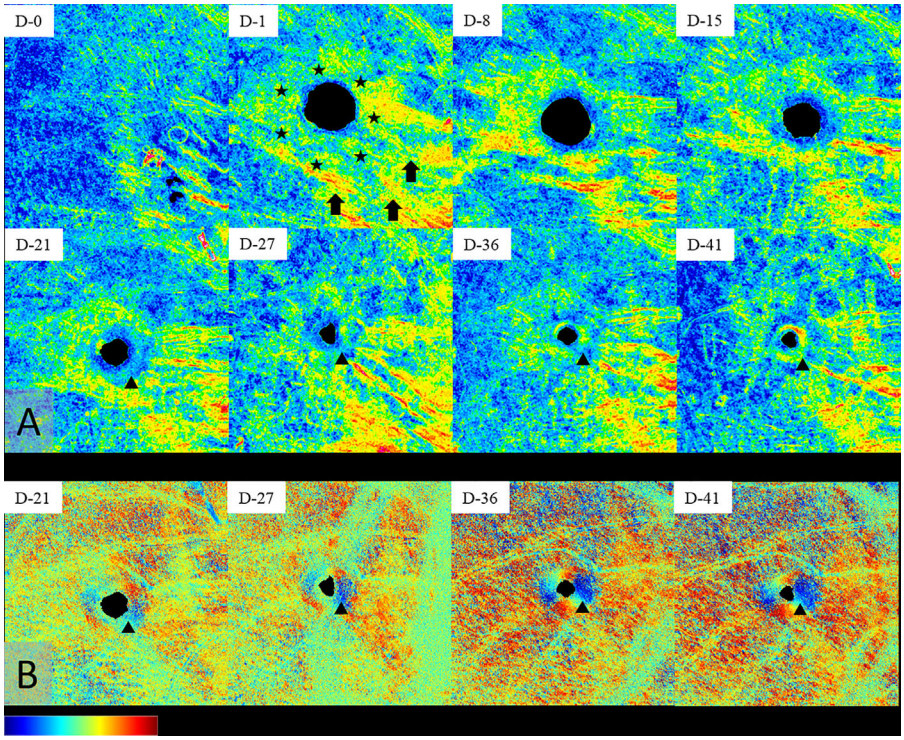

Fig. 5. Time-lapse PS-OCT imaging of tissue region covering a tissue wound on the mouse pinna. (**a**) *En face* phase retardation map on day 0–41 and (**b**) *en face* axis orientation map on day 21–41. In Figure 5a, after onset of the wound, the increase of phase retardation values in the vicinity of wound (stars and arrows) is visible. However, since day 21, the gradual increment of the phase retardation and the optic axis vales (arrow heads) is also seen in the rim of wound (re-grown tissue) as the wound is closing. FOV of all images is $5 \times 5\,\text{mm}^2$. The color scale of the phase retardation and the relative axis orientation are ranged from 0° to 75° and from -90° to $+90^\circ$, respectively.

appeared to be stretched out (at day 1, 8, and 15) and contracted back to baseline (on day 41). The behavior of phase retardation in the wound-free region is elusive to explain in the current research scope. Images at bottom row are *en face* relative axis orientation mapping of intermediate depth of the tissue.

DISCUSSION AND CONCLUSIONS

We have demonstrated a multifunctional imaging for monitoring wound healing in the mouse pinna. This work is a preliminary study on multifunctional imaging application of PS-OCT for wound healing. After generating the 1-mm-diameter wound in the mouse pinna with a complete biopsy punch, we observed over 6 weeks structural and vascular alterations surrounding the wound area as well as anisotropic tissue variations using a swept source PS-OCT system, spanning inflammation and proliferation stages of wound healing. When the tissues are damaged, usually blood clotting (hemostasis) occurs to the injured site and followed by inflammation to initiate tissue repair. As the symptoms of the inflammation, thickened epidermal tissue (tissue swelling) and vasodilation and its resulting increased blood perfusion were manifested in OCT and OMAG images on a 1-day post-wounding (Figs. 3 and 4), which responses are similar to injury with the previous investigations [37,54,55]. Afterwards, the proliferative phase was observable through the wound with newly grown tissue (granulation tissue), into which new networks of blood vessels develop, a process known as angiogenesis from OMAG images after 1-week post-wounding. Moreover, PS-OCT images showed the increase of the phase retardation and highly oriented collagen direction in the granulation tissue since 3-weeks post-wounding. The increment in these birefringence properties is most likely due to deposition and realignment of collagen in the regenerated tissue (see Fig. 5). In Figure 3, we showed asymmetric tissue growth during wound healing. The proximal tissue was grown faster. However, the accurate grown direction of the fastest grown tissue was right side below the image. Interestingly, this fastest growth direction is consistent with the direction for which the pattern like strand heads as shown in Figure 5. It is not clear which one of this pattern or geometrical vessel distribution surrounding the wound is actively involved in anisotropic tissue growth. However, this could be investigated in the future study using PS-OCT.

For visualizing features provided by PS-OCT, we measured the phase retardation and the optic axis at a certain depth (above auricular cartilage) below the mouse pinna surface. We observed that the phase retardation value was notably increased in the tissue area around the wound after wound induction as shown in Figure 5a. However, this increase may be due to either the change in a local birefringence or diattenuation within the tissues, or both. Direct measurements of the local birefringence and the diattenuation [56–59] are necessary to identify the origin of the retardation change. Since PS-OCT system used in this study utilized a single input polarization state with fiber optics, it is not possible to fully measure polarization properties, which makes accurate analysis of the obtained PS-OCT signal difficult. Future study is warranted to employ PS-OCT with two input polarization states to accurately measure a depth-localized phase retardation that is independent of the tissue diattenuation.

In summary, we observed and analyzed wound healing of the tissue in the mouse pinna with multiple information including structural changes (OCT image), birefringence distribution and orientation changes of collagen structure (PS image), and vessel network images. The results indicate that multiple complementary information may offer a chance to see a more comprehensive picture of wound healing. We also believe that the multifunctional imaging approach of PS-OCT would be useful for dermatology such as tissue aging study, drug development for wound healing and cosmetic industry.

ACKNOWLEDGMENT

The work was supported in part by National Institutes of Health grants (R01HL093140 and R01EB009682).

REFERENCES

1. Huang D, Swanson E, Lin C, et al. Optical coherence tomography. Science 1991;254(5035):1178–1181.
2. Tomlins PH, Wang RK. Theory, developments and applications of optical coherence tomography. J Phys D: Appl Phys 2005;38(15):2519–2535.
3. Costa RA, Skaf M, Melo LAS, et al. Retinal assessment using optical coherence tomography. Prog Retin Eye Res 2006;25(3):325–353.
4. Sattler E, Kästle R, Welzel J. Optical coherence tomography in dermatology. J Biomed Opt 2013;18(6):061224.
5. Qin J, Jiang JY, An L, Gareau D, Wang RK. In vivo volumetric imaging of microcirculation within human skin under psoriatic conditions using optical microangiography. Lasers Surg Med 2011;43(2):122–129.
6. Todea C, Negrutiu ML, Balabuc C, et al. Optical coherence tomography applications in dentistry. Timisoara Med J 2010;60(1):5–17.
7. Maldonado RS, Mettu P, El-Dairi M, Bhatti MT. The application of optical coherence tomography in neurologic diseases. Neurol Clin Pract 2015;5(5):460–469.
8. Bezerra HG, Costa MA, Guagliumi G, Rollins AM, Simon DI. Intracoronary optical coherence tomography: A comprehensive review. JACC Cardiovasc Interv 2009;2(11):1035–1046.
9. Kirtane TS, Wagh MS. Endoscopic optical coherence tomography (OCT): Advances in gastrointestinal imaging. Gastroenterol Res Pract 2014;2014:1–7.
10. Wang RK, Hurst S. Mapping of cerebro-vascular blood perfusion in mice with skin and skull intact by Optical Micro-AngioGraphy at 13 μm wavelength. Opt Express 2007;15(18):11402.
11. Zhang A, Zhang Q, Chen C-L, Wang RK. Methods and algorithms for optical coherence tomography-based angiography: A review and comparison. J Biomed Opt 2015; 20(10):100901.
12. Chen C-L, Wang RK. Optical coherence tomography based angiography [Invited]. Biomed Opt Express 2017;8(2):1056.
13. Chen Z, Milner TE, Srinivas S, et al. Noninvasive imaging of *in vivo* blood flow velocity using optical Doppler tomography. Opt Lett 1997;22(14):1119.
14. Leitgeb RA, Werkmeister RM, Blatter C, Schmetterer L. Doppler optical coherence tomography. Prog Retin Eye Res 2014;41:26–43.

15. Jung YR, Reif R, Zeng YG, Wang RK. Three-dimensional high-resolution imaging of gold nanorods uptake in sentinel lymph nodes. Nano Lett 2011;11(7):2938–2943.
16. Wang C, Kim J, Jin C, Leong P, McEwan A. Review: Near infrared spectroscopy in optical coherence tomography. J Infrared Spectrosc 2012;20(1):237.
17. Wang RK, Kirkpatrick S, Hinds M. Phase-sensitive optical coherence elastography for mapping tissue microstrains in real time. Appl Phys Lett 2007;90(16):164105.
18. Larin KV, Sampson DD. Optical coherence elastography-OCT at work in tissue biomechanics [Invited]. Biomed Opt Express 2017;8(2):1172.
19. Ambrozinski L, Song S, Yoon SJ, et al. Acoustic micro-tapping for non-contact 4D imaging of tissue elasticity. Sci Rep 2016;6:38967.
20. Kennedy BF, Wijesinghe P, Sampson DD. The emergence of optical elastography in biomedicine. Nat Photonics 2017; 11(4):215–221.
21. Wang RK, Jacques SL, Ma Z, Hurst S, Hanson SR, Gruber A. Three dimensional optical angiography. Opt Express 2007; 15(7):4083.
22. Yousefi S, Qin J, Wang RK. Super-resolution spectral estimation of optical micro-angiography for quantifying blood flow within microcirculatory tissue beds in vivo. Biomed Opt Express 2013;4(7):1214.
23. Hee MR, Swanson EA, Fujimoto JG, Huang D. Polarization-sensitive low-coherence reflectometer for birefringence characterization and ranging. J Opt Soc Am B 1992; 9(6):903.
24. de Boer JF, Hitzenberger CK, Yasuno Y. Polarization sensitive optical coherence tomography—A review [Invited]. Biomed Opt Express 2017;8(3):1838.
25. Fan C, Wang Y, Wang RK. Spectral domain polarization sensitive optical coherence tomography achieved by single camera detection. Opt Express 2007;15(13):7950.
26. Park BH, Saxer C, Srinivas SM, Nelson JS, de Boer JF. In vivo burn depth determination by high-speed fiber-based polarization sensitive optical coherence tomography. J Biomed Opt 2001;6(4):474.
27. Kim KH, Pierce MC, Maguluri G, et al. In vivo imaging of human burn injuries with polarization-sensitive optical coherence tomography. J Biomed Opt 2012;17(6):066012.
28. Gong P, Chin L, Es'haghian S, et al. Imaging of skin birefringence for human scar assessment using polarization-sensitive optical coherence tomography aided by vascular masking. J Biomed Opt 2014;19(12):126014.
29. Lo WCY, Villiger M, Golberg A, et al. Longitudinal, 3D imaging of collagen remodeling in murine hypertrophic scars *in vivo* using polarization-sensitive optical frequency domain imaging. J Invest Dermatol 2016;136(1):84–92.
30. Ponticorvo A, Burmeister DM, Rowland R, et al. Quantitative long-term measurements of burns in a rat model using spatial frequency domain imaging (SFDI) and laser speckle imaging (LSI). Lasers Surg Med 2017;49(3):293–304.
31. Lau P, Bidin N, Islam S, et al. Influence of gold nanoparticles on wound healing treatment in rat model: Photobiomodulation therapy. Lasers Surg Med 2017;49(4):380–386.
32. Yafi A, Muakkassa FK, Pasupneti T, et al. Quantitative skin assessment using spatial frequency domain imaging (SFDI) in patients with or at high risk for pressure ulcers. Lasers Surg Med 2017;49(9):827–834.
33. Wang Y, Gutierrez-Herrera E, Ortega-Martinez A, Anderson RR, Franco W. UV fluorescence excitation imaging of healing of wounds in skin: Evaluation of wound closure in organ culture model. Lasers Surg Med 2016;48(7):678–685.
34. Padilla-Martinez JP, Wang R, Franco W. Evaluation of cell and matrix mechanics using fluorescence excitation spectroscopy: Feasibility study in collagen gels containing fibroblasts. Lasers Surg Med 2016;48(4):377–384.
35. Oh J-T, Lee S-W, Kim Y-S, Suhr K-B, Kim B-M. Quantification of the wound healing using polarization-sensitive optical coherence tomography. J Biomed Opt 2006;11(4):041124.
36. Yousefi S, Qin J, Dziennis S, Wang RK. Assessment of microcirculation dynamics during cutaneous wound healing phases *in vivo* using optical microangiography. J Biomed Opt 2014;19(7):076015.
37. Qin W, Baran U, Wang R. Lymphatic response to depilation-induced inflammation in mouse ear assessed with label-free optical lymphangiography: Lymphatic response to depilation-induced inflammation. Lasers Surg Med 2015; 47(8):669–676.
38. Wang H, Baran U, Wang RK. In vivo blood flow imaging of inflammatory human skin induced by tape stripping using optical microangiography: *In vivo* blood flow imaging of inflammatory human skin. J Biophotonics 2015; 8(3):265–272.
39. Park BH, Pierce MC, Cense B, de Boer JF. Real-time multi-functional optical coherence tomography. Opt Express 2003; 11(7):782.
40. Park BH, Pierce MC, Cense B, et al. Real-time fiber-based multi-functional spectral-domain optical coherence tomography at 1.3 μm. Opt Express 2005;13(11):3931–3944.
41. Li E, Makita S, Hong Y-J, Kasaragod D, Yasuno Y. Three-dimensional multi-contrast imaging of *in vivo* human skin by Jones matrix optical coherence tomography. Biomed Opt Express 2017;8(3):1290.
42. Augustin M, Fialová S, Himmel T, et al. Multi-functional OCT enables longitudinal study of retinal changes in a VLDLR knockout mouse model. Georgakoudi I, ed. PLoS ONE 2016;11(10):e0164419.
43. Sugiyama S, Hong Y-J, Kasaragod D, et al. Birefringence imaging of posterior eye by multi-functional Jones matrix optical coherence tomography. Biomed Opt Express 2015; 6(12):4951.
44. Bonesi M, Sattmann H, Torzicky T, et al. High-speed polarization sensitive optical coherence tomography scan engine based on Fourier domain mode locked laser. Biomed Opt Express 2012;3(11):2987.
45. Götzinger E, Baumann B, Pircher M, Hitzenberger CK. Polarization maintaining fiber based ultra-high resolution spectral domain polarization sensitive optical coherence tomography. Opt Express 2009;17(25):22704.
46. Yousefi S, Zhi Z, Wang RK. Eigendecomposition-based clutter filtering technique for optical microangiography. IEEE Trans Biomed Eng 2011;58(8):2316–2323.
47. Zhang Q, Wang J, Wang RK. Highly efficient eigen decomposition based statistical optical microangiography. Quant Imaging Med Surg 2016;6(5):557–563.
48. Götzinger E, Pircher M, Sticker M, Fercher AF, Hitzenberger CK. Measurement and imaging of birefringent properties of the human cornea with phase-resolved, polarization-sensitive optical coherence tomography. J Biomed Opt 2004;9(1):94.
49. Wang RK, Xu XQ, He YH, Elder JB. Investigation of optical clearing of gastric tissue immersed with hyperosmotic agents. IEEE J Sel Top Quantum Electron 2003; 9(2):234–242.
50. Xu X, Wang RK. The role of water desorption on optical clearing of biotissue: studied with near infrared reflectance spectroscopy. Med Phys 2003;30(6):1246–1253.
51. Kirsner RS, Eaglstein WH. The wound healing process. Dermatol Clin 1993;11(4):629–640.
52. Yin X, Chao JR, Wang RK. User-guided segmentation for volumetric retinal optical coherence tomography images. J Biomed Opt 2014;19(8):086020.
53. Hirshberg A, Lib M, Kozlovsky A, Kaplan I. The influence of inflammation on the polarization colors of collagen fibers in the wall of odontogenic keratocyst. Oral Oncol 2007; 43(3):278–282.
54. Jung Y, Dziennis S, Zhi Z, Reif R, Zheng Y, Wang RK. Tracking dynamic microvascular changes during healing after complete biopsy punch on the mouse pinna using optical microangiography. Kano MR, ed. PLoS ONE 2013;8(2): e57976.
55. Yousefi S, Qin J, Zhi Z, Wang RK. Label-free optical lymphangiography: Development of an automatic segmentation method applied to optical coherence tomography to visualize lymphatic vessels using Hessian filters. J Biomed Opt 2013;18(8):086004.

56. Hyle Park B, Pierce MC, Cense B, de Boer JF. Jones matrix analysis for a polarization-sensitive optical coherence tomography system using fiber-optic components. Opt Lett 2004;29(21):2512.
57. Jiao S, Yu W, Stoica G, Wang L. Optical-fiber-based Mueller optical coherence tomography. Opt Lett 2003;28(14): 1206–1208.
58. Kemp NJ, Zaatari HN, Park J, Rylander HG, III, Milner TE. Form-biattenuance in fibrous tissues measured with polarization-sensitive optical coherence tomography (PS-OCT). Opt Express 2005;13(12):4611–4628.
59. Makita S, Yamanari M, Yasuno Y. Generalized Jones matrix optical coherence tomography: Performance and local birefringence imaging. Opt Express 2010;18(2):854.